Chemical Science

ROYAL SOCIETY OF CHEMISTRY

EDGE ARTICLE

View Article Online
View Journal

Cite this: DOI: 10.1039/d6sc02701f

All publication charges for this article have been paid for by the Royal Society of Chemistry

A robust Au–C≡C anchoring group greatly improves the signal stability of electrochemical aptamer-based sensors for *in vivo* measurements

Wanxue Zhang,[a] Bandar Alsuwayni,[bc] Jiamei Liu,[a] Qingqing Wu,[b] Ziyin Mei,[a] Songjun Hou,[b] Zishuo Zhang,[a] Xuewei Du,[a] Suyan Yi,[a] Shaoguang Li,*[a] Colin Lambert,*[b] Hui Li*[a] and Fan Xia

Received 1st April 2026
Accepted 13th April 2026

DOI: 10.1039/d6sc02701f

rsc.li/chemical-science

The ability to monitor drug pharmacokinetics in real time and directly *in vivo* is critical to achieve therapeutic efficacy and personalized medicine. Electrochemical aptamer-based (EAB) sensors have emerged as a promising platform for this purpose, yet their long-term stability is compromised by the degradation of the conventional Au–S bond-based bioelectronic interface under continuous interrogation. To address this fundamental limitation, we introduced an approach based on an Au–C≡C anchoring group to create a significantly more robust sensing interface. This stable configuration enabled our sensors to retain 92% signal integrity over 72 hours (>6000 scans) in whole blood. Leveraging this exceptional stability, we successfully achieved real-time tracking of drug concentrations in live rats, demonstrating a significant advance toward continuous pharmacokinetic monitoring.

Introduction

Medical devices that enable continuous, *in vivo* monitoring, as an emerging technology capable of tracking specific target substances in a real-time fashion are being developed, thus providing great opportunities for clinical use.[1–4] However, current biomedical devices for *in vivo* measurement of, for example, oxygen,[5] glucose,[6] or lactate,[7,8] are limited in scope, as they predominantly rely on highly specific enzyme-based reactions. Such inherent limitation creates a significant gap in addressing the broader spectrum of unmet monitoring needs. EAB sensors are promising candidates for filling this role. They utilize aptamers as recognition probes, which possess several merits including low cost, high stability, and ease of chemical modification.[9–11] EAB sensors utilize the conformational changes of such aptamers upon recognition of target analytes, thereby generating easily measurable electrochemical signals and are applicable for a great variety of analytes.[12,13] When EAB sensors undergo continuous, real-time monitoring, particularly in complex media, they suffer from signal decay which does not reflect the target concentration accurately. Such decay stems from multiple factors, including nuclease degradation of the DNA probe, electrode surface biofouling, instability of anchoring chemistry, *etc*.[14,15]

Recent studies have indeed been complicated by signaling decay challenges.[16] For example, Leung *et al.* demonstrated the use of artificial nucleic acids as a probe instead of the natural ones to greatly improve the nuclease-resistant ability, thus achieving an enhanced signal stability for their EAB sensors *in vivo*.[17] Relevantly, our group developed a pH-stable redox reporter as a stable indicator for EAB sensors deployed in bladder in living rats.[18] From the aspect of biofouling, our previous work demonstrated that protective hydrogels and immobilized self-assembled monolayers (SAMs) can also reduce biofouling and thus current drift.[19,20] Soh and colleagues developed a biomimetic multicomponent biosensor coated with polymers to prevent fouling, which enables continuous measurement of specific target molecules *in vivo*.[21] Complementing these approaches, recent studies have introduced polymer brushes as robust antifouling layers to extend sensor lifetimes in complex media,[22] while zwitterionic SAMs have been shown to effectively resist nonspecific adsorption and improve discrimination against chemical analogues.[23] In parallel, there are many studies, including those from our group, on the development of a calibration-free algorithm to reduce the electrochemical sensing signals with optimized performance in complex matrices.[24–28]

The above-described efforts significantly improve the signal stability, while they don't tackle the problem of probe detachment, which will ultimately cause the sensor to fail. Accordingly, many studies explored new anchoring chemistry by

[a]*State Key Laboratory of Geomicrobiology and Environmental Changes, Engineering Research Center of Nano-Geomaterials of Ministry of Education, Faculty of Materials Science and Chemistry, China University of Geosciences, Wuhan 430074, China. E-mail: lisg@cug.edu.cn; lihui-chem@cug.edu.cn*

[b]*Lancaster University, Faculty of Science and Technology, Lancaster University Department of Physics, Lancaster LA1 4YB, England, UK. E-mail: c.lambert@lancaster.ac.uk*

[c]*University of Hail, Faculty of Science, Physics Department, Kingdom of Saudi Arabia*

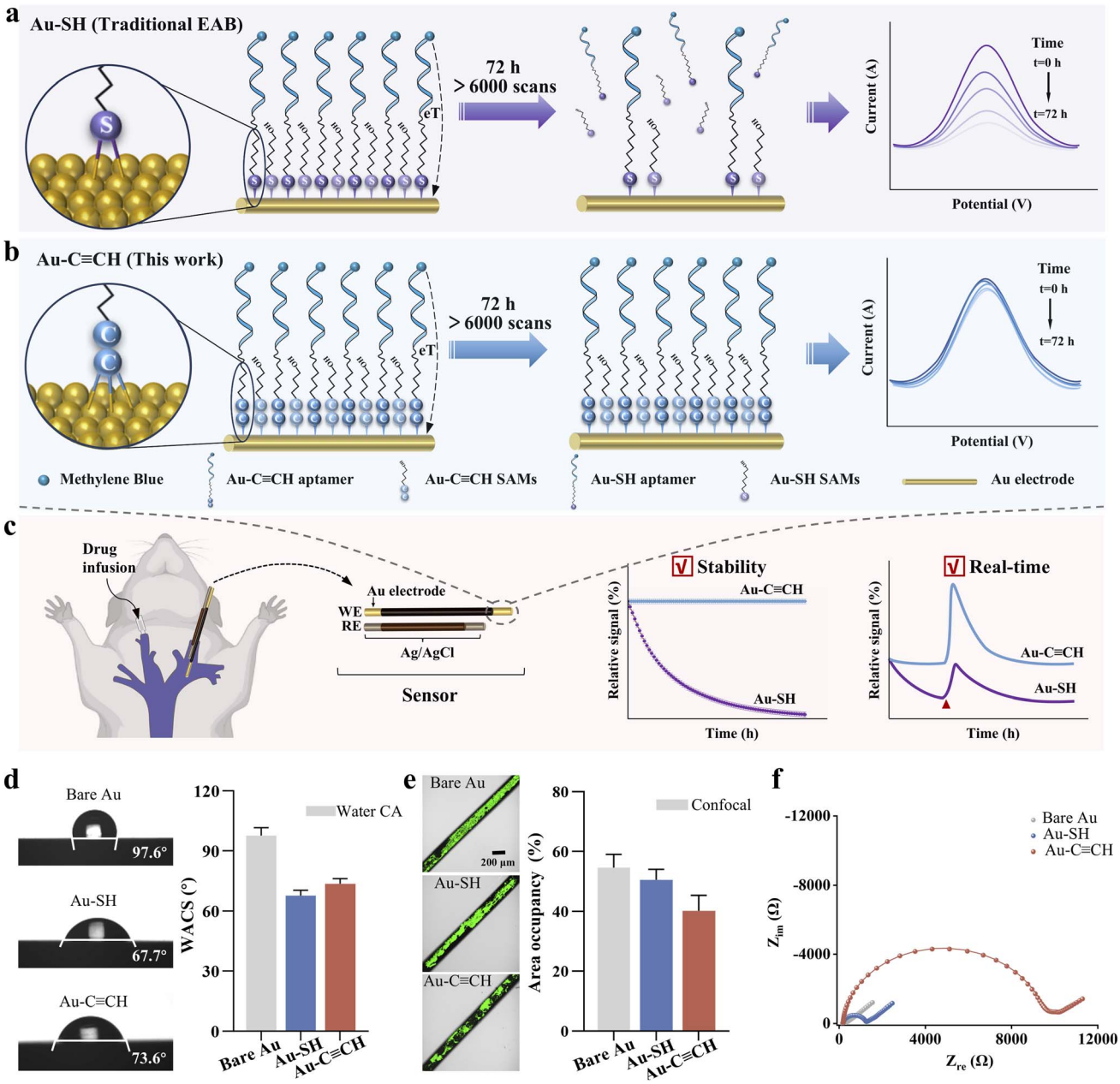

Fig. 1 Aptamers are anchored to the electrode surface through alkyne-based anchoring to form Au–C≡C-based EAB sensors with excellent stability. (a) Schematic illustration of the stability of traditional Au–SH-based EAB sensors and (b) Au–C≡CH-based sensors exhibiting better stability. (c) Implantation of the high-performance Au–C≡CH-based EAB sensors *in vivo* enables more stable real-time drug monitoring. (d) Wettability of the sensor surface before and after blood treatment. (e) The antifouling properties of sensors using confocal fluorescence microscopy studies. (f) Electrochemical impedance spectra of the sensors.

replacing the mostly conventional Au–S anchoring groups, including Au–N, Au–Se, C–C, C–N, *etc.*[29–32] because thiol SAMs can be replaced by biological thiols in complex physiological environments,[33] which causes signal decay for these sensors.[15,34] It is worth noting that alkanethiol SAMs themselves can remain stable under carefully controlled, narrow electrochemical potential windows.[15] However, for applications requiring wider potential windows or prolonged interrogation, the inherent instability of the Au–S bond itself becomes a limiting factor. A very recent study introduced a gold–alkyne immobilization chemistry for DNA probe into EAB sensors,[35] while the majority of the self-assembled monolayer (SAM) remained composed of conventional thiolated backfillers (*e.g.*, 6-mercaptohexanol). As we and others have demonstrated, the long-term stability of EAB sensors is critically dependent on the integrity of both the probe and SAM. Our work here introduces a complete alkyne-based interfacial architecture, wherein both the aptamer probe and the SAM-forming diluent are anchored *via* Au–C≡C bonds (Fig. 1a and b). This holistic strategy eliminates the vulnerability associated with residual Au–S linkages, resulting in

Table 1 A summary of the stability performance of EAB sensors (note: signal retention = $i/i_0 \times 100\%$)

	Buffer			Blood			
	72 h	6000 scans	Signal retention	8 h	6000 scans	Signal retention	*In vivo*
Supramolecular electro-chemical aptamer[39]	No	No	—	Yes	—	77%	No
Alkanethiol monolayer end groups[40]	No	—	—	No	No	—	No
Agarose hydrogel protective layer[19]	No	No	—	Yes	—	95%	No
AuNPs@MXene nanocomposite[41]	No	—	—	No	No	—	No
Xenonucleic acids[17]	No	—	—	No	No	—	Yes
Carboxylate-terminated electrode[42]	No	—	—	Yes	—	50%	No
Surface-confined DNA monolayers[43]	No	—	—	No	No	—	No
8-Mercapto-1-octanol and zwitterionic polybetaine hydrogel[44]	Yes	Yes	81%	No	No	—	No
Software approach for redox peak tracking[45]	Yes	No	80%	No	No	—	No
Biomimetic phosphatidylcholine-terminated monolayer[46]	No	—	—	Yes	—	90%	Yes
This work: Au–C≡C anchoring group	**Yes**	**Yes**	**92%**	**Yes**	**Yes**	**94%**	**Yes**

substantially enhanced stability compared to partial replacement approaches. Ultimately, we can achieve real-time and stable molecular monitoring in complex samples and even *in vivo* environments, with the evidenced use of the Au–C≡C anchor for constructing conductive molecular layers and a highly ordered monolayer onto the surface.[36–38]

We summarize here the stability performance of various EAB sensors with the above-described strategies when they are deployed in buffer, whole blood, and even *in vivo* conditions (Table 1). The sensor developed in this work, which utilizes the Au–C≡C anchoring group, distinguishes itself by maintaining >90% signal retention in both whole blood and *in vivo* environments over 72 hours, representing the only technology demonstrating high stability under all tested conditions.

Results and discussion

We hypothesized that the Au–C≡C bond, formed by alkyne anchoring groups, would confer superior stability to EAB sensors compared to conventional Au–S bonds, owing to its higher binding strength (Fig. 1). To evaluate this, we fabricated sensors using both alkyne- and thiol-anchored DNA probes along with the corresponding self-assembled monolayers (SAMs). We selected 5-heptyne-1-ol (HYO) as the alkyne-anchored analogue to the traditional thiol-based monolayer 6-mercapto-1-hexanol (MCH). This pairing ensured that the two SAMs differed only in their anchoring chemistry (alkyne *vs.* thiol), while being matched in the terminal functional group and alkyl chain length. The alkyne-anchored group not only substantially enhanced the operational stability of the EAB sensors under continuous measurement in both *in vitro* and *in vivo* settings but also yielded improved sensitivity and reliability of the sensing devices.

Both Au–C≡C and Au–S interfaces differ in the surface properties, including contact angles, antifouling properties and electrochemical impedance spectra. First, the HYO-based surface exhibited a similar contact angle to MCH, as both molecules possess the same –OH terminal group. HYO exhibited a lower amount of absorbed protein (*i.e.*, higher antifouling capability) than the MCH monolayer (surface coverage values of 40.2% *versus* 50.6%, respectively). Electrochemical impedance spectroscopy (EIS) determined the surface coverage associated with monolayer structural integrity.[47,48] We observed a 10-fold higher resistance value for the HYO-based surface than MCH-based ones (10 701.3 Ω *vs.* 1109.2 Ω). We observed that the resistance value and surface coverage of alkyne-based molecules were both higher than those of MCH, which might be related to the surface adsorption of the molecules. This is consistent with the previous work reporting that the electrode surfaces anchored with gold–alkyne molecules exhibited the highest adsorption coverage compared to those from gold–sulfur and gold–selenium bonds[36] (Table S1).

Model compounds for the demonstration of stability

To comparatively evaluate the interfacial stability of Au–C≡C and Au–S anchors under electrochemical interrogation, we synthesized model compounds MB–C≡CH and MB–SH and fabricated redox-active SAMs to simulate sensor operation (Fig. 2, S1–S5). We assessed the stability of these SAMs using complementary techniques: long-term electrochemical cycling quantified the retention of the redox signal, X-ray photoelectron spectroscopy (XPS) monitored the chemical integrity of the interface at critical intervals, and confocal laser scanning microscopy visualized the spatial distribution and retention of the molecular layer over time.

Under continuous electrochemical scanning over 72 hours (~1200 scans), the signal of MB–C≡CH functionalized electrodes remain quite stable with less than 10% of fluctuations, while MB–SH exhibited a significant loss (*ca.* ~60%) of its original peak current (Fig. 2c). To probe the degradation mechanism, we analyzed both electrodes at selected intervals (t = 0, 24, 48, 72 h) using XPS and confocal microscopy, tracking the temporal evolution of chemical composition and spatial distribution of both SAMs.

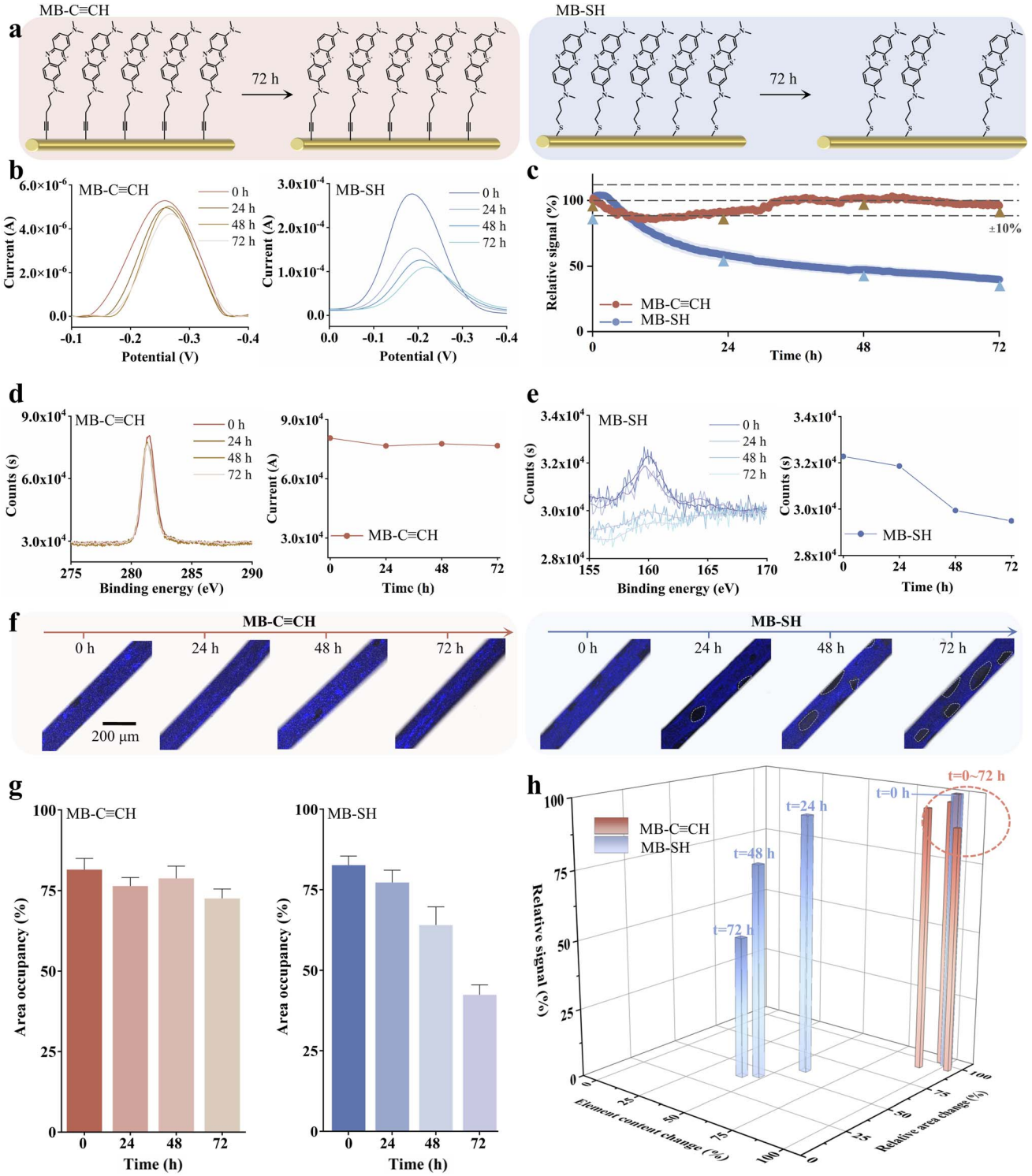

Fig. 2 The Au–C≡C bond enhances the stability of immobilized molecules on the electrode surface. (a) We first used model compounds to fabricate their respective MB–C≡CH (left panel) and MB–SH (right panel) to demonstrate the stability of these two SAMs. (b) Baseline-subtracted square-wave voltammograms of MB–C≡CH and MB–SH, respectively. (c) MB–C≡CH supports longer continuous electrochemical interrogation in PBS buffer compared to MB–SH. (d) X-ray photoelectron spectra (XPS) of the MB–C≡CH peak of C 1s after electrochemical interrogation at 0, 24, 48, and 72 h in PBS buffer. (e) XPS spectra of the MB–SH peak of S 2p after electrochemical interrogation at 0, 24, 48, and 72 h in PBS buffer. (f and g) Confocal microscopy images and the respective surface coverage of MB–C≡CH– and MB-SH–based surfaces. (h) Summary of temporal variations in fluorescence surface coverage, SWV signal change, and XPS results.

XPS results demonstrate that such decrease of the MB signal is due to the loss of SAMs over time. Specifically, the MB–C≡CH SAMs revealed two distinct peaks in the C 1s spectrum at 281.4 eV and 282.8 eV (Fig. S6), which are assigned to the Au–C bond (C 1s, sp^3 carbon) and the terminal C≡C bond (C 1s, sp carbon), respectively, according to the previous literature.[36,49,50] Critically, the intensity of the 282.8 eV peak remained stable throughout electrochemical interrogation (Fig. 2d), demonstrating the robust chemical integrity of the Au–C≡C anchoring bond. Conversely, the MB–SH SAMs showed the characteristic double peak in the S 2p region (Fig. 2e), with the S $2p_{3/2}$ component at 160.0 eV corresponding to the Au–S bond[51] (Fig. S6). We observed a significant, time-dependent decrease in the integrated area of this S $2p_{3/2}$ peak during sensor operation. This indicates progressive desorption of thiol-anchored molecules from the gold surface. This marked contrast to the invariant C 1s signal intensity of the MB–C≡CH SAMs provides direct spectroscopic evidence of the superior interfacial stability conferred by the alkyne anchoring chemistry.

Leveraging the intrinsic fluorescence of methylene blue (MB), we employed confocal laser scanning microscopy to comparatively assess the interfacial stability of both MB–C≡CH and MB–SH SAMs at selected intervals (t = 0, 24, 48, 72 h) (Fig. 2f and S7). Quantitative analysis of the integrated fluorescence area revealed the remaining MB molecules on the interface. The MB–C≡CH SAMs demonstrated exceptional stability with over 90% of MB molecules remaining on the surface during electrochemical interrogation over 72 hours (Fig. 2g and S8). In sharp contrast, the MB–SH-modified surface exhibited significant time-dependent fluorescence loss, with ~50% of MB molecules remaining on the surface over the same period.

Collective evidence from electrochemical, XPS spectroscopic, and confocal microscopy analyses consistently demonstrates the superior stability of alkyne-anchored (MB–C≡CH) SAMs over conventional thiol-based (MB–SH) monolayers under sustained electrochemical interrogation. These results provide direct visual and quantitative evidence that gold–alkyne bonds confer superior resistance to electrochemical perturbation, effectively minimizing probe detachment compared to conventional gold–thiol bonds.

The stability of Au–C≡C anchored EAB sensors

Following the stability studies that demonstrated the superiority of Au–C≡C anchoring groups over thiol counterparts in the model compound (Fig. 2 and S9), we then fabricated EAB sensors using vancomycin (VAN)-binding aptamers as the first test bed (Fig. 3a and b). Similar to the model compound, here we also selected the 72 hour time point to assess the intrinsic stability of the sensing interface in a simple buffer solution over an extended period without the confounding factor of sample degradation. As expected, VAN–C≡CH-functionalized sensors exhibited <10% peak current attenuation under continuous electrochemical interrogation in PBS (72 h, >6000 cycles), whereas thiol-anchored sensors underwent significant signal loss similar to the interrogation and complete signal loss (*i.e.*, current drop to zero) after 55 h (Fig. 3c). Of note, the alkyne-anchored EAB sensor exhibited a packing density (1.20×10^{11} molecules per cm^2) that is one order of magnitude lower than that of thiol-anchored ones (1.38×10^{12} molecules per cm^2), which reproduces the results reported in a recent study.[35]

Next, we further interrogated our sensors in a complex matrix (*e.g.*, whole blood). Specifically, we interrogated our sensors in the undiluted whole blood matrix for 8 hours, as it extends beyond the typical maximum duration of *in vivo* electrophysiological recordings (approximately 6 hours in anesthetized rat models), thereby allowing us to evaluate sensor stability under physiologically relevant, complex matrix conditions. Once again, the alkyne-anchored sensor (VAN–C≡CH) exhibited a more stable peak current in the voltammograms compared to the thiol-anchored sensor (VAN–SH). Over a monitoring period of 8 hours (>700 cycles), the peak current of VAN–C≡CH sensors only decreased by less than 15%, while that of VAN–SH-based sensors dropped by approximately 90%.

To elucidate the mechanism underlying signal attenuation in the whole blood environment, we implemented a urea wash protocol to discriminate between biofouling-induced signal loss and irreversible probe detachment. This experimental rationale posits that signal recovery should occur post-wash if attenuation stems primarily from nonspecific biomolecular adsorption. Contrary to this expectation, thiol-anchored (VAN–SH) sensors exhibited no signal regeneration following urea treatment. We achieved a robust and repetitive titration curve after the urea wash in comparison to that prior to washing (Fig. S10). This observation conclusively demonstrates that signal degradation originates predominantly from permanent desorption of aptamer probes from the electrode surface, rather than reversible biofouling. Notably, alkyne-anchored EAB sensors maintained ~85% signal integrity post-wash, and we observed no signal recovery of thiol-anchored sensors, further validating that the signal decrease is due to the loss of probe rather than biofouling challenges.

As it is true for the two model compounds (MB–SH *vs.* MB–C≡CH), we performed XPS measurements to monitor interfacial compositional evolution during electrochemical interrogation at key timepoints (t = 0, 2, 4, 8 h). Likewise, the C 1s spectrum at 286.2 eV of the VAN–C≡CH surface can be assigned to the terminal C≡C bond (C 1s, sp carbon) (Fig. S11). Critically, the intensity of this peak remained stable throughout electrochemical interrogation (Fig. 3f), demonstrating the robust chemical integrity of the Au–C≡C anchoring bond. Conversely, the VAN–SH SAMs exhibited a characteristic double peak in the S 2p region (*e.g.*, peaked at 162.9 eV), which exhibited a significant, time-dependent decrease in the integrated area during sensor operation. Remarkably, we observed that the decrease in magnitude matched well with the decay of electrochemical signals. At t = 2, 4 and 8 h, both XPS and electrochemical currents for thiol-based sensors exhibited signal decreases of ~70%, ~80% and ~90%, respectively. This indicates progressive desorption of thiol-anchored molecules from the gold surface.

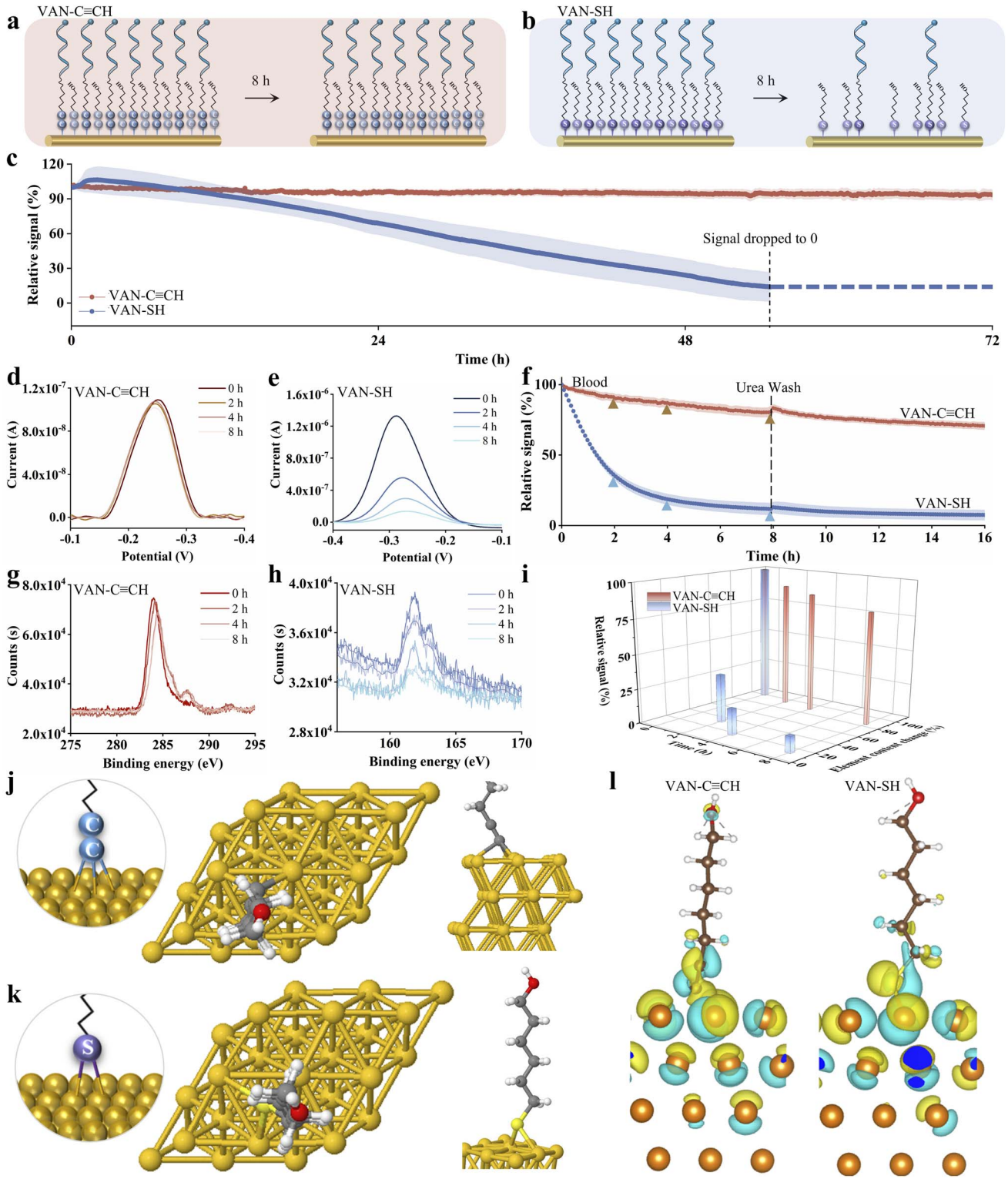

Fig. 3 Au–C≡C-based EAB sensors exhibit excellent electrochemical stability. We utilized vancomycin-modified EAB sensors to illustrate this effect. (a) Schematic representation of the VAN–C≡CH sensor and (b) the VAN–SH sensor during 8 h of electrochemical access in blood. (c) Au–C≡C supports longer continuous electrochemical interrogation in PBS buffer compared to Au–SH. (d) Baseline-subtracted square-wave voltammograms of VAN–C≡CH and (e) VAN–SH over 8 hours. (f) We investigated whether the observed signal decay in blood was due to aptamer detachment by exposing both sensors to blood for 8 hours while performing electrochemical scans, followed by washing the electrodes with 9.5 M urea, which only recovered a small portion of the lost signal. (g) C 1s X-ray photoelectron spectroscopy of VAN–C≡CH at 0, 2, 4, and 8 h and (h) S 2p X-ray photoelectron spectroscopy of VAN–SH at 0, 2, 4, and 8 h in blood. (i) Summary of temporal variations in SWV signal change and the relative elemental content ratio. DFT simulation results showing top and lateral views of adsorption structures on the Au surface: (j) Au–CC at the fcc hollow site and (k) Au–S at the bridge site. (l) The corresponding charge density difference maps for –C≡C– and –S anchored molecules on Au surfaces≡≡ exhibited a more-dense charge distribution at the bonding interfaces of HYO than that of MCH, highlighting its stronger electronic coupling.

We further evaluated the signaling stability of aptamer–monolayer complexes formed *via* different anchoring chemistries. Specifically, we compared co-assembled monolayers employing vancomycin aptamers with either thiol (VAN–SH) or terminal alkyne (VAN–C≡CH) anchors, assembled alongside hydroxyl-terminated alkanethiol (HYO) or mercaptohexanol (MCH) diluents, respectively. The results revealed that the configuration utilizing gold–alkyne anchor groups for both the aptamer and SAM formation exhibited superior stability at the electrode interface (Fig. S12). The configuration of Au–SH for both components exhibited the lowest signals over the same durations. The sensors with mixed anchoring components (VAN–SH/HYO or VAN–C≡CH/MCH) lied in between.

To further assess the generality of the alkyne-anchoring strategy, we fabricated sensors using aptamers for kanamycin (KAN) and doxorubicin (DOX). Consistent with our hypothesis, the Au–C≡C-anchored sensors for both targets exhibited superior stability, sustaining less than 20% signal loss over 8 hours. In contrast, their Au–SH counterparts suffered a substantial signal loss of 60–80% under identical conditions (Fig. S12).

Theoretical study

In order to elucidate the above experimental observations, density functional theory (DFT) calculations were performed using the Vienna *Ab initio* Simulation Package (VASP)[52] to investigate both the geometric and electronic structures of the system. A four-layer (3 × 3) Au (111) surface was modelled with lateral dimensions of 8.85 Å × 8.85 Å, and a 4 × 4 × 1 *k*-point mesh was employed for Brillouin zone sampling (see more computational details in the Theoretical Methods section and Fig. S13 of the supplementary information (SI)). Our simulation results indicate that HYO exhibits a preference for fcc hollow site adsorption over the bridge site and hcp hollow site energetically (Fig. 3j) with an adsorption energy E_{ads} of −3.66 eV. Bader charge analysis[53–56] reveals that HYO gains approximately 0.20 electrons upon adsorption (Fig. 3l, Table S2). Other adsorption sites were systematically examined for both HYO and MCH molecules (see Fig. S14–S16 for more details). MCH exhibits a similar adsorption preference to HYO, favoring the bridge site (Fig. 3k) with an adsorption energy of −2.32 eV. This suggests that the –S anchor forms a weaker bonding with the Au surface compared to the Au–C≡C– anchor in HYO. Bader charge analysis further shows that 0.08 electrons are transferred to MCH electrons from gold substrates. To gain deeper insight into the interfacial interactions, charge density difference (CDD) properties were further investigated for the charge distribution between the surface and the molecules (Fig. 3l). The denser charge distribution at the molecule–substrate interface for HYO highlights a stronger electronic coupling compared to MCH. Collectively, the stronger adsorption energy and larger charge transfer and denser CDD features collectively indicate that Au–C≡C-anchored sensors exhibit superior electronic coupling and are likely to perform more efficiently than thiol-anchored counterparts.

Sensor performance

Based on the theoretical studies, we speculate that Au–C≡C-anchored sensors exhibit faster charge transfer rates than the Au–SH-based ones. To investigate this, we used cyclic voltammetry (CV) to examine their electrochemical behavior (Fig. 4a, b and S17). According to Laviron's theory, the relationship between the anodic peak potential (E_{pa}), cathodic peak potential (E_{pc}), and scan rate v under a diffusionless electron transfer (ET) mechanism is given by eqn (1) (ref. 57):

$$\Delta E_p = 2.3RT/(1-\alpha)nF \lg v + 2.3RT/(1-\alpha)nF \lg((1-\alpha)nF/(RTK_s)) \quad (1)$$

In eqn (1), ΔE_p is the peak-to-peak separation of the redox potential, α is the electron transfer coefficient, K_s is the electron transfer rate constant, n is the number of electrons transferred ($n = 2$ for the MB molecule in this study), F is Faraday's constant, T is the temperature (Kelvin), and R is the gas constant. The electron transfer coefficient α is calculated as follows:

$$\alpha = S_a/(S_a - S_c) \quad (2)$$

where S_a and S_c are the slopes of the linear relationships E_{pa}–log v and E_{pc}–log v, respectively.

The standard electron transfer rate constants (K_s) calculated for the VAN–C≡CH and VAN–SH sensors were determined to be 2.84 s^{-1} and 2.52 s^{-1}, respectively. This confirms that the alkyne-based anchoring strategy enhances the interfacial electron transfer kinetics. This finding is further corroborated by frequency-dependent studies, where the peak charge transfer frequency for the VAN–C≡CH sensor exhibits a distinct shift toward higher frequencies compared to the VAN–SH analogue (160 Hz *vs.* 18 Hz) (Fig. 4c). The consistency between the enhanced K_s values and the increased characteristic frequency provides robust evidence for improved charge transfer efficiency *via* the alkyne linkage. We further tested the kanamycin- and doxorubicin-detecting sensors, achieving higher transfer kinetics for alkyne sensors. For the former, we achieved the K_s values calculated for the C≡CH- and SH-anchored sensors as 3.22 s^{-1} and 2.64 s^{-1}, respectively (Fig. S18). For the latter, we observed an even higher K_s of 3.42 s^{-1} for alkyne-anchored sensors, while a similar value for SH-anchored ones (2.60 s^{-1}). These results demonstrate that using Au–C≡C bonding can effectively enhance the signal transfer kinetics of EAB sensors.

The alkyne-anchored sensors also exhibited varied target affinity in comparison to the conventional EAB sensors. For example, the VAN–C≡CH sensor demonstrated 4-fold lower affinity against vancomycin in PBS buffer with a dissociation constant (K_D value) of 162 μM. In contrast, the VAN–SH sensor exhibited a K_D value of 40 μM (Fig. 4g and S20). To decouple the effects of anchoring groups from those of probe density, we also compared thiol-anchored sensors fabricated at similarly low densities (*via* controlled backfilling). These low-density thiol sensors also exhibited rapid binding kinetics and affinities as alkyne-anchored sensors with similar densities (Fig. S21).

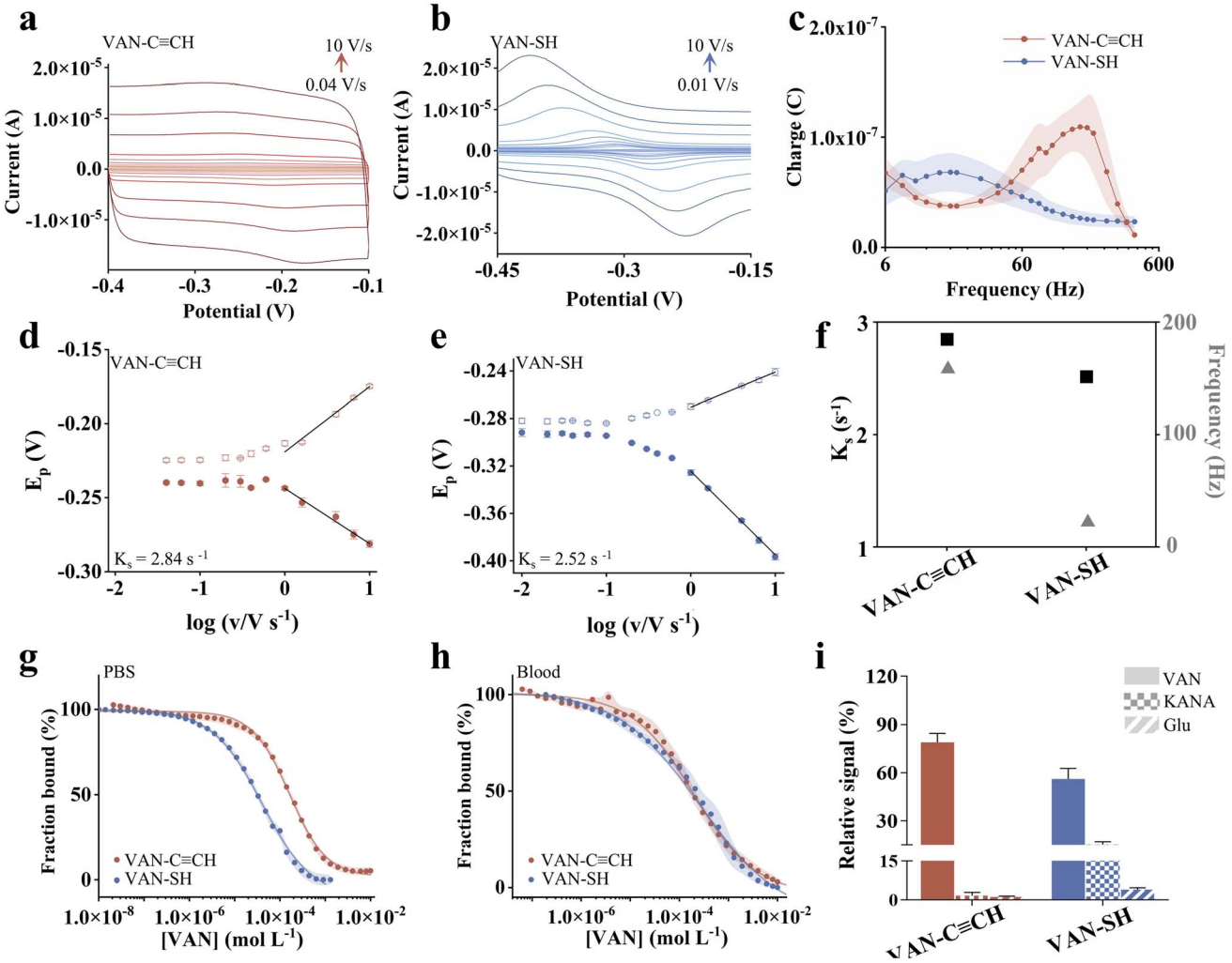

Fig. 4 The Au–C≡C anchor group accelerates the charge transfer between MB and the electrode surface. (a) Cyclic voltammograms (CVs) recorded at VAN–C≡CH and (b) VAN–SH electrodes in PBS buffer at scan rates ranging from 0.01 to 10 V s^{-1} (the zoomed-in view of plots of (a) and (b) are shown in Fig. S17). (c) Function of charge transfer *versus* frequency. Relationship between the peak potential and the logarithm of scan rate for (d) VAN–C≡CH and (e) VAN–SH, respectively. (f) Comparison of charge transfer rates obtained using two different calculation methods. Titration curves of the sensor in (g) PBS and (h) whole blood. (i) Specificity analysis of the sensors.

Similarly, when deployed in blood, the alkyne-based sensors exhibited slightly higher affinity than thiol-based ones (197 μM *vs.* 261 μM) (Fig. 4h). Notably, both classes of sensors exhibited good specificity against targets in comparison to the interferent molecules. Likewise, KAN-detecting sensors exhibited comparable target affinity for both anchoring chemistry in PBS buffer, while when deployed in serum or blood thiol-based sensors achieved higher affinities. DOX-detecting sensors exhibited lower affinities (*i.e.*, greater K_D values) for C≡CH in comparison to SH-anchored ones (Fig. S22, Table S3).

We previously demonstrated that the terminal groups of SAMs manipulated the sensor performance including stability, affinity, specificity, *etc.*,[20,24,58,59] particularly for sensors deployed in the complex matrix. In order to expand the alkyne-anchoring SAMs, here we prepared a series of alkyne monolayers with the same alkyl segment and varied terminal groups bearing non-charge or charge moieties (Fig. 5a), thus altering the wettability, antifouling property and ultimately sensor performance. These included mono-charged molecules such as 5-heptynoic acid (HA) and L-propargylglycine hydrochloride (HPGH), zwitterionic derivatives such as 5-heptyne-1-phosphatidylcholine (HPC) (Fig. S23 and 24) and 5-heptyne-1-amine hydrochloride (HYAH), and non-charged molecules such as 1-heptyne (HY), 5-heptyne-1-ol (HYO), and 1H-perfluoro-1-octyne (PFOY).

Wettability characteristics of the as-prepared SAMs are greatly dependent on their terminal groups (Fig. 5b, Table S4).[20,58,60] As expected, the fluoro-substituted derivative PFOY forms the most hydrophobic SAMs among all these derivatives with a contact angle of 91.6°, followed by HPGH of 89.6°. The methyl-terminated molecule HY exhibits a contact angle of 80.5°. SAMs fabricated from charged terminal group-based derivatives have significantly lower contact angles ranging from 65.4° to 74.3°. Similar to our previous observations,[20,58] we also demonstrated a significant alteration of hydrophilicity when

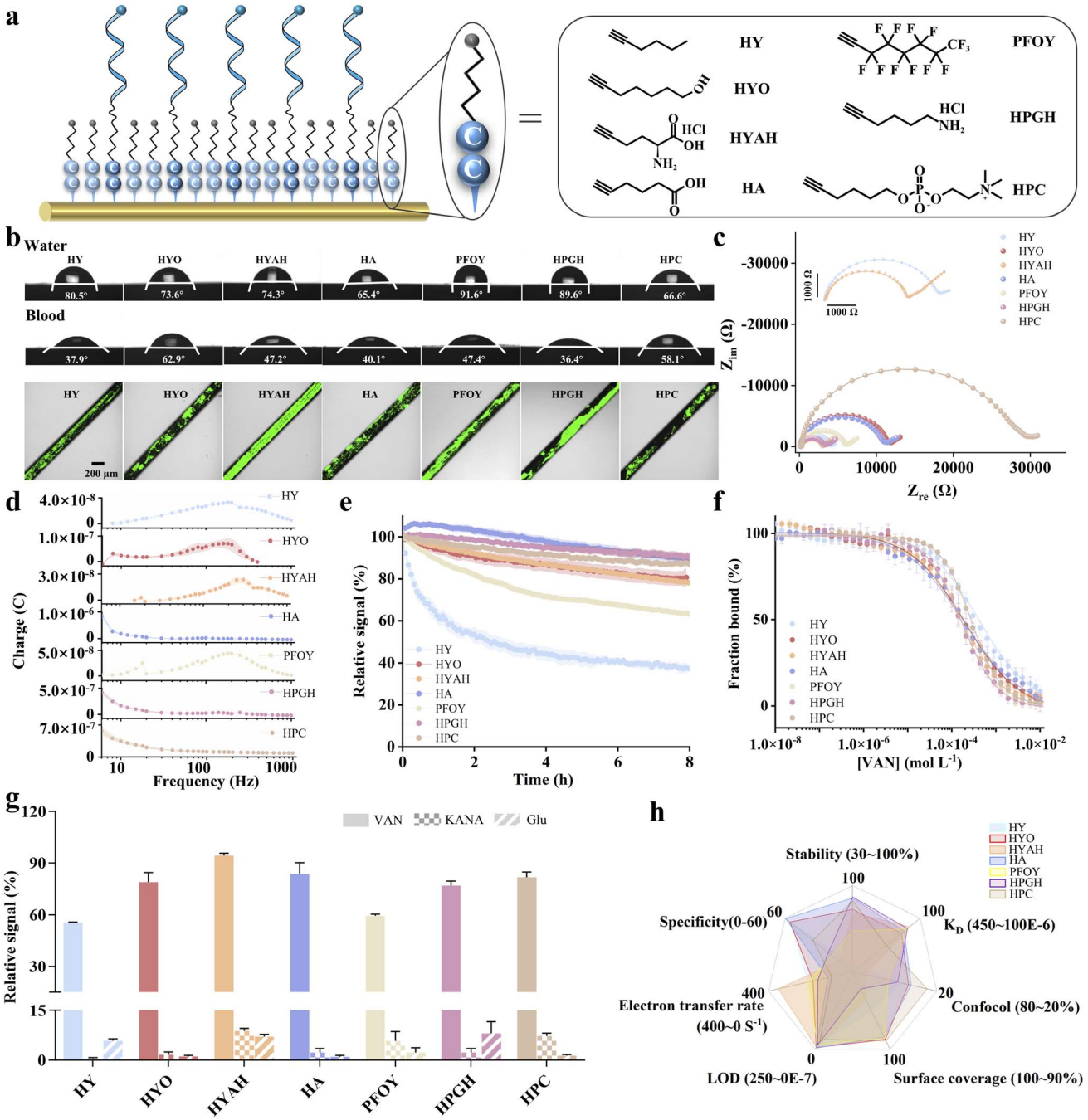

Fig. 5 We comprehensively evaluated the performance of EAB sensors constructed using seven different SAMs, all anchored *via* a stable Au–C≡C bond. (a) Schematic illustration of the vancomycin aptamer anchored *via* the Au–C≡C bond and the molecular structures of various SAMs. (b) Wettability study (top) and confocal fluorescence microscopy images (down) of electrodes prepared with different SAMs. (c) Impedance spectra of electrodes. (d) The charge transfer study of sensors fabricated with various SAMs. (e) Signal stability of EAB sensors fabricated with different SAMs in whole blood. (f) Titration curves of the sensors in whole blood. (g) Specificity analysis of the sensors. (h) Radar plots were used to evaluate the overall performance of these SAMs and their corresponding sensors.

immersing our electrodes with SAMs in blood, a real sample matrix for target analysis. We observed greater CA changes for hydrophobic surfaces than that for hydrophilic ones. For instance, both hydrophilic SAMs from HYO and HPC achieved a minimal decrease of CA value by 8.5°–10.7°. Membranes with single charges (HA and HYAH) exhibited moderate decreases in contact angle after blood treatment, with changes of 25.3° and 27.1°, respectively. Hydrophobic SAMs from HY, PFOY and HPGH exhibited greatest decreases in CA value by 42.6°, 44.2° and 53.2°, respectively.

The structural characteristics of SAMs significantly influence their antifouling capabilities. Among the tested SAMs, HYAH monolayers exhibited the highest adsorption of proteins, with an area occupancy (Aroc) value of 70.9%, attributed to the

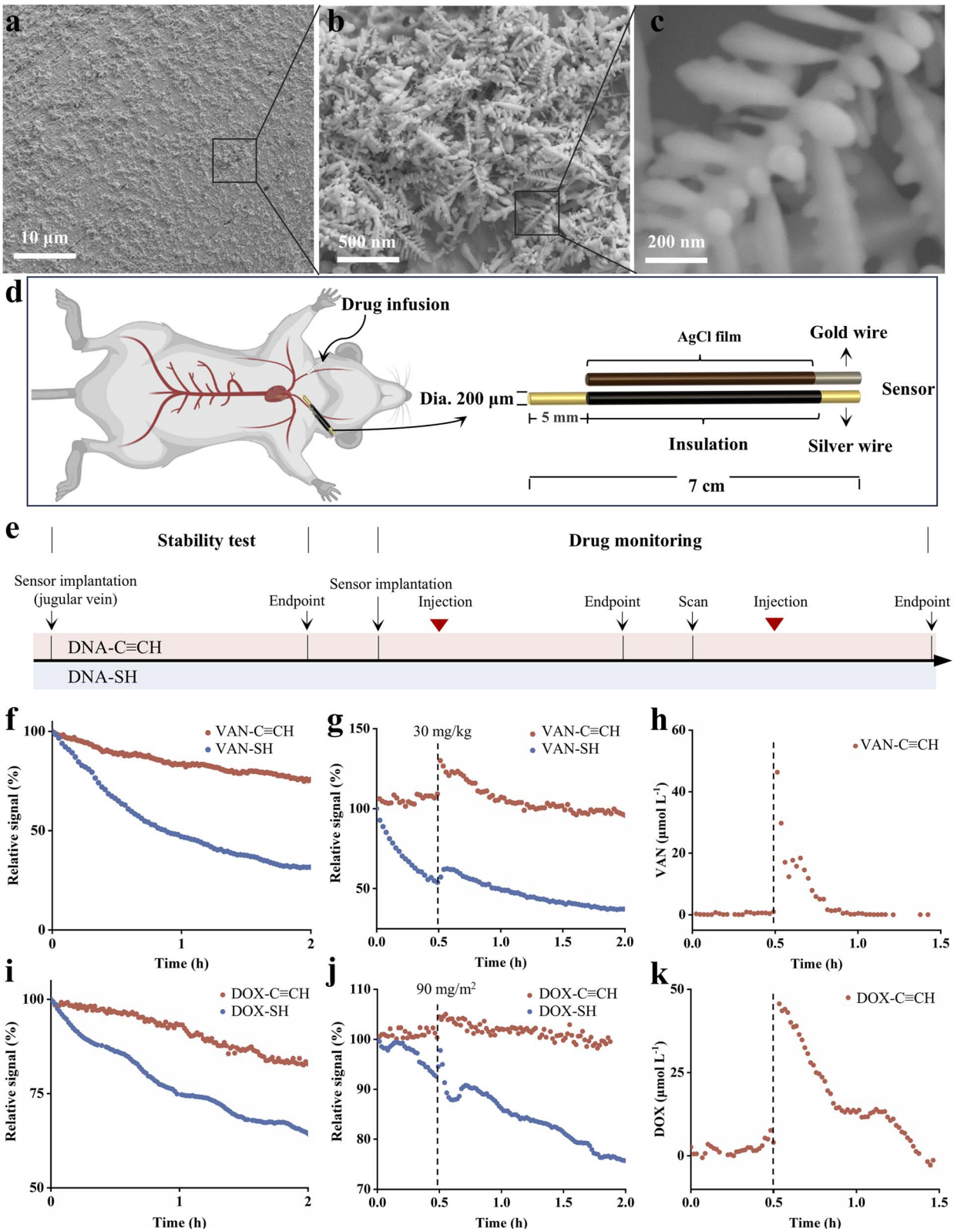

Fig. 6 Real-time monitoring of vancomycin and doxorubicin using an *in vivo* electrochemical aptamer sensor. (a–c) Gold electrodes undergo electrochemical etching to form nanodendritic structures, enhancing the electroactive surface area and increasing the aptamer grafting density. (d) Schematic of the implanted sensor structure, implantation site, and drug injection process. (e) We monitored the *in vivo* stability of the sensor along with the monotonic increase in intravenous dosage. Stability of the (f) vancomycin sensor and (i) doxorubicin sensor after implantation. (g) Plasma vancomycin concentration returns to baseline following first-order elimination kinetics after intravenous injection of 30 mg kg^{-1} vancomycin. (j) Plasma doxorubicin concentration follows a similar trend after intravenous injection of 90 mg m^{-2} doxorubicin. Time-dependent concentration profiles of (h) vancomycin and (k) doxorubicin.

electrostatic attraction between the charged SAMs and BSA proteins with a net negative charge.[58] In contrast, the negatively charged molecular HA showed a significantly reduced adsorption with an Aroc value of 38.3%. The zwitterionic HPC demonstrated the lowest Aroc value of ~27.0%, demonstrating its best antifouling capability. Among non-charged molecules, the most hydrophobic monolayer, PFOY, exhibited the highest area occupancy ratio (*e.g.*, 54.7%), followed by HPGH and HY, with Aroc values of 47.9% and 45.3%, respectively.

Next, we employed electrochemical impedance spectroscopy (EIS) using ferrocyanide as a redox probe to assess the surface coverage and structural integrity.[47,48] All the impedance plots exhibit a low-frequency straight line and a very small semicircle in the high-frequency region (Fig. 5c, Table S4), indicating a diffusion-controlled process for the redox pair present on the bare Au surface. The derivatives of our SAMs have the same length of hydrophobic alkyl region but vary in the head group. The greater head groups produced a higher R_{ct}. HPC with greatest head groups exhibited the maximum R_{ct} value of 20 872 Ω, followed by HA with a R_{ct} of 10 554 Ω. Next, PFOY exhibited a R_{ct} value of 7081 Ω. The HY-, HYAH- and HPGH-based SAMs with smallest heading groups (–H) exhibited the lowest R_{ct} value in the range of 3000 to 4000 Ω.

We determined the electron transfer rate of sensors fabricated from these monolayers by analyzing the square wave voltammetry frequency at maximum charge transfer (Fig. 5d and Table S5). Likewise, the structural characteristics of SAMs significantly influence their electron transfer capabilities. HYAH exhibited the fastest electron transfer rate of 354 s^{-1}, followed by HY and PFOY.[61] The model compound HYO also achieved a moderate electron transfer kinetic. Mono-charged SAMs including HA and HPGH exhibited extremely slow electron transfer kinetics without a maximum over the range of 6–1000 Hz. The zwitterionic HPC monolayer also exhibited no maximum, probably due to the larger heading groups of molecules which lower the electron transfer efficiency.

Upon validation of surface properties, we then tested our sensors fabricated from alkyne-anchored SAMs in whole blood, observing that sensor performance (*e.g.*, stability, affinity and specificity) is greatly dependent of the terminal structures. Sensors fabricated from HA, HPGH, and HPC exhibited the highest stability, with signal attenuation of less than 20% after a period of 8 hours, followed by HYAH-based sensors with signal reductions of 21.8%, respectively. PFOY-based sensors exhibited moderate stability, with a signal loss of approximately 36.7%, while HY exhibited the lowest signal attenuation at ~62.6%. HY-based sensors exhibited the lowest target affinity (Fig. 5f and S26 and Table S5), with a dissociation constant (K_D) of 416.7 μM, followed by HPC-based sensors with a K_D value of 275.9, while all the other sensors exhibited a similar target affinity with K_D values in the range of 150–200 μM.

Specificity characteristics of the as-prepared sensors are greatly dependent on the terminal groups of these alkyne SAMs. The HA- and HY-based sensors exhibited the highest specificity for vancomycin, with average of specificity factor (SEF_{ave}) values of ~59 and 55, respectively, indicating that the signal changes caused by kanamycin and glucose were significantly smaller than those caused by vancomycin. The SEF_{ave} values for HYO and HPC were 55 and 35, respectively, while the remaining sensors possessed SEF_{ave} values of <25.

To understand the factors governing these performance differences, we examined the properties of each alkyne-anchored SAM using the polygon area. While all share the same Au–C≡C anchoring chemistry, their terminal groups vary in hydrophilicity, antifouling capability, and structural compactness. Our analysis suggests that the overall sensor performance is primarily driven by antifouling properties and hydrophilicity under continuous electrochemical interrogation. Terminal groups with moderate hydrophilicity (*e.g.*, HYO and HA) effectively reduce nonspecific adsorption and maintain stable interfacial integrity under bias, yielding the highest overall scores. In contrast, highly hydrophobic or bulky terminal groups (*e.g.*, HPGH and HYAH) compromise surface coverage and baseline stability, while groups with insufficient antifouling characteristics (*e.g.*, PFOY) exhibit a greater signal drift in complex media. Electron-transfer kinetics and target partitioning also contribute to sensitivity differences but play a secondary role here, as all alkyne-based interfaces retain sufficient conformational flexibility for aptamer function. Given the need to compare against the conventional benchmark SAM MCH, we selected HYO for further investigation in subsequent experiments.

Motivated by the *in vitro* stability, we then demonstrated the ability of Au–C≡C-based sensors for *in vivo* study in living animals (Fig. 6). To enhance the electrochemical surface area, the gold electrode surface was electrochemically etched to create a roughened microstructure, as corroborated by the scanning electron microscopy (SEM) images (Fig. 6a–c). Specifically, the sensors were placed in the external jugular vein of anesthetized Sprague-Dawley rats, with drug injections administered through the contralateral external jugular vein (Fig. 6d–k and S27). While the SH-based sensors exhibited severe baseline drift with signal losses of 70% and 36% for vancomycin- and doxorubicin-detecting sensors, respectively (Fig. 6f and i, blue traces). In contrast, both Au–C≡C-based sensors exhibited much greater signal stability with a signal loss of less than 20%. We then employed a non-compartmental analysis mode to fit the pharmacokinetics of vancomycin and doxorubicin. Following intravenous administration of vancomycin at a dose of 30 mg kg^{-1}, plasma concentrations increased rapidly, reaching a maximum concentration (C_{max}) of 46.33 μM and an elimination half-life ($t_{1/2}$) of 0.07955 hours. Similarly, intravenous administration of doxorubicin at a dose of 90 mg m^{-2} resulted in a peak plasma concentration of 45.61 μM and a terminal elimination half-life of 0.2719 hours. These results demonstrate that both compounds exhibit rapid distribution and elimination *in vivo*.

Conclusions

In this work, we present an electrochemical aptamer-based (EAB) sensor utilizing an Au–C≡C anchoring group, which significantly enhances operational stability and reduces baseline drift in complex biological environments such as whole

blood. Compared to conventional thiol-based interfaces, the Au–C≡C-modified sensors maintain high temporal resolution, low detection limits, and high accuracy while substantially improving signal integrity. We demonstrated the general applicability of such stable sensing platform through the continuous detection of three small-molecule drugs—doxorubicin, kanamycin, and vancomycin. Furthermore, the sensor was successfully deployed for real-time, *in situ* monitoring of doxorubicin and vancomycin in the jugular vein of living rats, underscoring its capability for reliable pharmacokinetic tracking *in vivo*. To elucidate the origin of the enhanced stability, density functional theory (DFT) calculations were performed, revealing a significantly higher adsorption energy for the Au–C≡C bond compared to the classical Au–S bond.

Our Au–C≡C anchoring strategy offers a versatile foundation for advanced implantable sensing technologies. Within the broader context of stable interfacial designs, alternative chemistries such as Au–Se-, Au–S-, and carbene-based anchors represent promising avenues for future exploration. Building on this stability of Au–C≡C-anchored EAB sensors, three key directions emerge for application-oriented development. First, this interface supports the design of sensors capable of multi-day to multi-month implantation for chronic conditions such as diabetes or gout. Second, it provides a platform to investigate and engineer interfacial interactions with evolving biological microenvironments. For instance, through covalent passivation or self-healing coatings, such sensor platform can maintain long-term signal fidelity. Third, its robustness facilitates the construction of multi-panel sensor arrays and expands the range of target molecules beyond those compatible with conventional Au–S chemistry. Beyond diagnostics, this anchoring strategy can be integrated into closed-loop bioelectronic therapeutics. For example, coupling Au–C≡C-anchored aptamer sensors with responsive polymer coatings or drug-releasing modules could achieve smart implants that autonomously regulate therapeutic delivery based on real-time biomarker levels, thereby bridging the gap between continuous monitoring and precision medicine.

Author contributions

Wanxue Zhang: performed the majority of the experimental operations, data acquisition, and processing; integrated and analyzed the datasets; and was responsible for drafting the initial manuscript as well as its subsequent revision and refinement. Bandar Alsuwayni: conducted the density functional theory (DFT) calculations, organized and analyzed the corresponding computational data, and contributed to writing the sections related to the theoretical studies. Jiamei Liu: assisted in the execution of partial experimental procedures, data acquisition, and processing. Qingqing Wu, Songjun Hou: jointly provided guidance on the DFT calculations and contributed to the revision of the manuscript. Ziyin Mei, Zishuo Zhan: jointly carried out the experiments and data processing related to testing alkynyl molecules with different terminal groups. Xuewei Du: responsible for parts of the *in vivo* experiments and for processing and analyzing the related data. Suyan Yi: assisted with data processing for part of the electrochemical measurements. Shaoguang Li, Colin Lambert, Hui Li (corresponding author): conceived and conceptualized the study, secured funding, provided resources, supervised and guided the project, validated the results, and critically reviewed and revised the manuscript. Fan Xia: secured funding, provided resources, supervised the project, and critically reviewed and revised the manuscript. All authors approved the final version of the manuscript.

Conflicts of interest

The authors have no conflicts to declare.

Data availability

Data are available from the corresponding author on reasonable request. Supplementary information (SI): detailed experimental conditions and the additional characterization of sensors and electrochemical sensor performance. See DOI: https://doi.org/10.1039/d6sc02701f.

Acknowledgements

This work was supported by Noncommunicable Chronic Diseases-National Science and Technology Major Project (2024ZD0531600), the National Natural Science Foundation of China (22474130, 22274144, 22090050, and U24A20502), the National Key Research and Development Program of China (2021YFA1200403), and the Natural Science Foundation of Shenzhen (JCYJ20220530162406014). This work was supported by the UK EPSRC programme grant QMol EP/X026876/1. The *in vivo* study was conducted in accordance with the Animal Care and Institutional Ethical Guidance in China. The experiment was authorized by the Animal Research Ethics Committee of Wuhan Cloud Clone Technology Co., Ltd (certificate number: IACU24-1359).

References

1 P. Dauphin-Ducharme, K. Yang, N. Arroyo-Currás, K. L. Ploense, Y. Zhang, J. Gerson, M. Kurnik, T. E. Kippin, M. N. Stojanovic and K. W. Plaxco, Electrochemical Aptamer-Based Sensors for Improved Therapeutic Drug Monitoring and High-Precision, Feedback-Controlled Drug Delivery, *ACS Sens*, 2019, **4**, 2832–2837.

2 J. Wang, Amperometric biosensors for clinical and therapeutic drug monitoring: a review, *J. Pharm. Biomed. Anal.*, 1999, **19**, 47–53.

3 R. S. Gaster, D. A. Hall, C. H. Nielsen, S. J. Osterfeld, H. Yu, K. E. Mach, R. J. Wilson, B. Murmann, J. Liao, S. S. Gambhir, *et al.*, Matrix-insensitive protein assays push the limits of biosensors in medicine, *Nat. Med.*, 2009, **15**, 1327–1332.

4 J. W. Seo, K. Fu, S. Correa, M. Eisenstein, E. A. Appel and H. T. Soh, Real-time monitoring of drug pharmacokinetics

within tumor tissue in live animals, *Sci. Adv.*, 2022, **8**, eabk2901.

5 H. Ren, M. A. Coughlin, T. C. Major, S. Aiello, A. R. Pena, R. H. Bartlett and M. E. Meyerhoff, Improved in Vivo Performance of Amperometric Oxygen (PO_2) Sensing Catheters via Electrochemical Nitric Oxide Generation/Release, *Anal. Chem.*, 2015, **87**, 8067–8072.

6 H. Yoon, X. Xuan, S. Jeong and J. Y. Park, Wearable, robust, non-enzymatic continuous glucose monitoring system and its in vivo investigation, *Biosens. Bioelectron.*, 2018, **117**, 267–275.

7 O. M. Schuvailo, O. O. Soldatkin, A. Lefebvre, R. Cespuglio and A. P. Soldatkin, Highly selective microbiosensors for in vivo measurement of glucose, lactate and glutamate, *Anal. Chim. Acta*, 2006, **573**, 110–116.

8 E. Fernandes, A. Ledo and R. M. Barbosa, Design and Evaluation of a Lactate Microbiosensor: Toward Multianalyte Monitoring of Neurometabolic Markers In Vivo in the Brain, *Molecules*, 2022, **27**, 514.

9 T. Hermann and D. J. Patel, Biochemistry - Adaptive recognition by nucleic acid aptamers, *Science*, 2000, **287**, 820–825.

10 A. Porchetta, A. Vallée-Bélisle, K. W. Plaxco and F. Ricci, Using Distal-Site Mutations and Allosteric Inhibition To Tune, Extend, and Narrow the Useful Dynamic Range of Aptamer-Based Sensors, *J. Am. Chem. Soc.*, 2012, **134**, 20601–20604.

11 Y. Wu and K. W. Plaxco, On the Design, Fabrication, and Operation of Electrochemical Aptamer-Based Sensors, *ACS Sens.*, 2025, **10**, 7218–7230.

12 B. R. Baker, R. Lai, M. S. Wood, E. H. Doctor, A. J. Heeger and K. W. Plaxco, An electronic, aptamer-based small-molecule sensor for the rapid, label-free detection of cocaine in adulterated samples and biological fluids, *J. Am. Chem. Soc.*, 2006, **128**, 3138–3139.

13 N. Arroyo-Currás, J. Somerson, P. A. Vieira, K. L. Ploense, T. E. Kippin and K. W. Plaxco, Real-time measurement of small molecules directly in awake, ambulatory animals, *Proc. Natl. Acad. Sci. U.S.A.*, 2017, **114**, 645–650.

14 J. D. Pham, L. C. Fetter, J. Gerson, T. E. Kippin, K. W. Plaxco and K. K. Leung, On the Blood Components Contributing to the Drift of Electrochemical Aptamer-Based Biosensors, *ACS Sens.*, 2025, **10**, 5160–5165.

15 K. K. Leung, A. M. Downs, G. Ortega, M. Kurnik and K. W. Plaxco, Elucidating the Mechanisms Underlying the Signal Drift of Electrochemical Aptamer-Based Sensors in Whole Blood, *ACS Sens*, 2021, **6**, 3340–3347.

16 G. F. Huldin, J. Huang and K. X. Fu, Nanoconfined constructs for electrochemical aptamer-based in vivo biosensing, *Curr. Opin. Electrochem.*, 2025, **51**, 101695.

17 K. K. Leung, J. Gerson, N. Emmons, J. M. Heemstra, T. E. Kippin and K. W. Plaxco, The Use of Xenonucleic Acids Significantly Reduces the In Vivo Drift of Electrochemical Aptamer-Based Sensors, *Angew. Chem., Int. Ed.*, 2024, **63**, e202316678.

18 S. Li, A. Ferrer-Ruiz, J. Dai, J. Ramos-Soriano, X. Du, M. Zhu, W. Zhang, Y. Wang, M. Herranz, L. Jing, *et al.*, A pH-independent electrochemical aptamer-based biosensor supports quantitative, real-time measurement in vivo, *Chem. Sci.*, 2022, **13**, 8813–8820.

19 S. Li, J. Dai, M. Zhu, N. Arroyo-Currans, H. Li, Y. Wang, Q. Wang, X. Lou, T. E. Kippin, S. Wang, *et al.*, Implantable Hydrogel-Protective DNA Aptamer-Based Sensor Supports Accurate, Continuous Electrochemical Analysis of Drugs at Multiple Sites in Living Rats, *ACS Nano*, 2023, **17**, 18525–18538.

20 Z. Zhang, Y. Wang, Z. Mei, Y. Wang, H. Li, S. Li and F. Xia, Incorporating Hydrophobic Moieties into Self-Assembled Monolayers to Enable Electrochemical Aptamer-Based Sensors Deployed Directly in a Complex Matrix, *ACS Sens*, 2022, **7**, 2615–2624.

21 Y. Chen, K. X. Fu, R. Cotton, Z. Ou, J. W. Kwak, J. C. Chien, V. Kesler, H. Y. Y. Nyein, M. Eisenstein and H. Tom Soh, A biochemical sensor with continuous extended stability in vivo, *Nat. Biomed. Eng.*, 2025, **9**, 1517–1530.

22 A. J. Trowbridge, G. F. Huldin, M. Pyo, K. M. Jordan, M. A. Rincon, T. Kim, M. J. Webber, H. Gao, C. H. Park and K. X. Fu, Zwitterionic Polymer Brushes Inside Nanoporous Gold Electrodes Enable Fouling-Resistant Electrochemical Biosensing, *ACS Appl. Polym. Mater.*, 2025, **7**, 15241–15254.

23 M. P. McGowan, A. J. Trowbridge, J. Reitemeier, K. M. Jordan and K. X. Fu, Surface charge effects of monovalent and zwitterionic monolayers to differentiate structurally similar aminoglycosides with electrochemical aptamer biosensors, *Biosens. Bioelectron.*, 2025, **276**, 117229.

24 H. Li, P. Dauphin-Ducharme, G. Ortega and K. W. Plaxco, Calibration-Free Electrochemical Biosensors Supporting Accurate Molecular Measurements Directly in Undiluted Whole Blood, *J. Am. Chem. Soc.*, 2017, **139**, 11207–11213.

25 M. Zhu, S. Li, H. Li, H. Li and F. Xia, Employing an Intercalated Redox Reporter in Electrochemical Aptamer-Based Biosensors to Enable Calibration-Free Molecular Measurements in Undiluted Serum, *Anal. Chem.*, 2020, **92**, 12437–12441.

26 Z. M. Chen, Q. Mou, S. H. Wu, Y. Xie, K. Salminen and J. J. Sun, Real-Time Tunable Dynamic Range for Calibration-Free Biomolecular Measurements with a Temperature-Modulated Electrochemical Aptamer-Based Sensor in an Unprocessed Actual Sample, *Anal. Chem.*, 2022, **94**, 1397–1405.

27 Z. M. Chen, Y. Wang, X. Y. Du, J. J. Sun and S. Yang, Temperature-Alternated Electrochemical Aptamer-Based Biosensor for Calibration-Free and Sensitive Molecular Measurements in an Unprocessed Actual Sample, *Anal. Chem.*, 2021, **93**, 7843–7850.

28 M. Zhu, C. Xie, F. Xu, S. Li, H. Li and F. Xia, Exploring Differential Electron Transfer Kinetics of Electrochemical Aptamer-Based Sensors to Achieve Calibration-Free Measurements, *ACS Sens*, 2025, **10**, 1105–1112.

29 S. Wang, X. Wang, F. Zhao and B. Zeng, Self-Powered PEC Cathodic Immunosensor for CA125 Detection Based on the Cu2O Photocathode and the CdS/PANI Photoanode, *ACS Sens.*, 2025, **23**, 351–358.

30 X. Li, X. Duan, L. Li, S. Ye and B. Tang, An accurate and ultrasensitive SERS sensor with Au-Se interface for bioimaging and in situ quantitation, *Chem. Commun.*, 2020, **56**, 9320–9323.
31 Z. Kadi, C. Slim and S. Griveau, Activation Methods of Carboxyl Functions for Enhanced Aptamer Immobilization on Glassy Carbon for Application to Electrochemical Biosensing, *Langmuir*, 2025, **41**, 4796–4805.
32 C. Corona-Elizarrarás, C. Slim, N. Arroyo-Currás, S. Griveau and S. Gutiérrez Granados, Surface Functionalization of Glassy Carbon Electrodes via Electrografting of Aminobenzoic Acid: A Proof-of-Concept Study for Aptasensor Design, *Electroanalysis*, 2025, **37**, e70082.
33 X. N. Gao, L. Jiang, B. Hu, F. Kong, X. Liu, K. Xu and B. Tang, Au-Se-Bond-Based Nanoprobe for Imaging MMP-2 in Tumor Cells under a High-Thiol Environment, *Anal. Chem.*, 2018, **90**, 4719–4724.
34 V. Clark, A. Prasad, Y. Yuan, E. Demek, F. Guzman, L. A. Garcia, P. S. Lukeman, B. Powell-Gray, J. Rodríguez-López and N. Arroyo-Currás, Extending the Operational Lifespan of Nucleic Acid-Based Electrochemical Sensors via Protection against Hydrogen Peroxide and Oligonucleotide Displacement, *ACS Sens*, 2025, **10**, 4945–4953.
35 L. A. Olivan, K. Hand and R. J. White, Utilization of Spontaneous Alkyne-Gold Self-Assembly Chemistry as an Alternative Method for Fabricating Electrochemical Aptamer-Based Sensors, *Langmuir*, 2024, **40**, 12117–12123.
36 C. Zhang, Z. Liu, L. Zhang, A. Zhu, F. Liao, J. Wan, J. Zhou and Y. Tian, A Robust Au-C≡C Functionalized Surface: Toward Real-Time Mapping and Accurate Quantification of Fe^{2+}in the Brains of Live AD Mouse Models, *Angew. Chem., Int. Ed.*, 2020, **59**, 20499–20507.
37 R. P. Weston, Y. Chen, T. J. Dzwonczyk, J. A. Veras, A. M. Sevigny and E. C. Landis, Electrically Transmissive and Stable Alkyne-Derived Molecular Layers on Nanoporous Gold, *J. Phys. Chem. C*, 2022, **126**, 9673–9682.
38 T. Zaba, A. Noworolska, C. M. Bowers, B. Breiten, G. M. Whitesides and P. Cyganik, Formation of Highly Ordered Self-Assembled Monolayers of Alkynes on Au(111) Substrate, *J. Am. Chem. Soc.*, 2014, **136**, 11918–11921.
39 S. Li, S. Miao, M. Chen, Y. Zhang, H. Li and F. Xia, Localized high probe density greatly improves the signaling stability of supramolecular electrochemical aptamer-based (Supra-EAB) sensors, *Chem. Commun.*, 2025, **61**, 274–277.
40 A. Shaver, S. D. Curtis and N. Arroyo-Currás, Alkanethiol Monolayer End Groups Affect the Long-Term Operational Stability and Signaling of Electrochemical, Aptamer-Based Sensors in Biological Fluids, *ACS Appl. Mater. Interfaces*, 2020, **12**, 11214–11223.
41 H. Duan, S. Tang, K. Goda and M. Li, Enhancing the sensitivity and stability of electrochemical aptamer-based sensors by AuNPs@MXene nanocomposite for continuous monitoring of biomarkers, *Biosens. Bioelectron.*, 2024, **246**, 115918.
42 R. M. Bakestani, Y. Wu, B. Glahn-Martinez, T. E. Kippin, K. W. Plaxco and R. W. Kolkman, Carboxylate-Terminated Electrode Surfaces Improve the Performance of Electrochemical Aptamer-Based Sensors, *ACS Appl. Mater. Interfaces*, 2025, **17**, 8706–8714.
43 M. Deng, M. Li, F. Li, X. Mao, Q. Li, J. Shen, C. Fan and X. Zuo, Programming Accessibility of DNA Monolayers for Degradation-Free Whole-Blood Biosensors, *ACS Mater. Lett.*, 2019, **1**, 671–676.
44 Z. Watkins, A. Karajic, T. Young, R. White and J. Heikenfeld, Week-Long Operation of Electrochemical Aptamer Sensors: New Insights into Self-Assembled Monolayer Degradation Mechanisms and Solutions for Stability in Serum at Body Temperature, *ACS Sens*, 2023, **8**, 1119–1131.
45 A. McHenry, M. Friedel and J. Heikenfeld, Voltammetry Peak Tracking for Longer-Lasting and Reference-Electrode-Free Electrochemical Biosensors, *Biosensors*, 2022, **12**, 782.
46 H. Li, P. Dauphin-Ducharme, N. Arroyo-Currás, C. H. Tran, P. A. Vieira, S. Li, C. Shin, J. Somerson, T. E. Kippin and K. W. Plaxco, A Biomimetic Phosphatidylcholine-Terminated Monolayer Greatly Improves the In Vivo Performance of Electrochemical Aptamer-Based Sensors, *Angew. Chem., Int. Ed.*, 2017, **56**, 7492–7495.
47 D. Li, X. Yu and Y. Dong, The different self-assembled way of n- and t-dodecyl mercaptan on the surface of copper, *Appl. Surf. Sci.*, 2007, **253**, 4182–4187.
48 V. Ganesh, S. K. Pal, S. Kumar and V. Lakshminarayanan, Self-assembled monolayers (SAMS) of alkoxycyanobiphenyl thiols on gold - A study of electron transfer reaction using cyclic voltammetry and electrochemical impedance spectroscopy, *J. Colloid Interface Sci.*, 2006, **296**, 195–203.
49 S. Zhang, K. L. Chandra and C. B. Gorman, Self-assembled monolayers of terminal alkynes on gold, *J. Am. Chem. Soc.*, 2007, **129**, 4876–4877.
50 S. Jeong, Y. Kwon, C. Park, Y. Ito, J. Park, M. S. Hwang, J. Chung and N. Sugita, Enhancing electrochemical performance of colorless polyimide-derived laser-induced graphene via gold nanoparticles integration: Towards advanced wearable and energy harvesting applications, *Nano Energy*, 2024, **126**, 109663.
51 T. M. Willey, A. L. Vance, T. van Buuren, C. Bostedt, L. J. Terminello and C. S. Fadley, Rapid degradation of alkanethiol-based self-assembled monolayers on gold in ambient laboratory conditions, *Surf. Sci.*, 2005, **576**, 188–196.
52 G. Kresse and J. Furthmuller, Efficiency of ab-initio total energy calculations for metals and semiconductors using a plane-wave basis set, *Comput. Mater. Sci.*, 1996, **6**, 15–50.
53 W. Tang, E. Sanville and G. Henkelman, A grid-based Bader analysis algorithm without lattice bias, *J. Phys.: Condens. Matter*, 2009, **21**, 084204.
54 E. Sanville, S. D. Kenny, R. Smith and G. Henkelman, Improved grid-based algorithm for Bader charge allocation, *J. Comput. Chem.*, 2007, **28**, 899–908.
55 G. Henkelman, A. Arnaldsson and H. Jónsson, A fast and robust algorithm for Bader decomposition of charge density, *Comput. Mater. Sci.*, 2006, **36**, 354–360.
56 M. Yu and D. R. Trinkle, Accurate and efficient algorithm for Bader charge integration, *J. Chem. Phys.*, 2011, **134**, 064111.

57 E. Laviron, General expression of the linear potential sweep voltammogram in the case of diffusionless electrochemical systems, *J. Electroanal. Chem.*, 1979, **101**, 19–28.
58 S. Li, Y. Wang, Z. Zhang, Y. Wang, H. Li and F. Xia, Exploring End-Group Effect of Alkanethiol Self-Assembled Monolayers on Electrochemical Aptamer-Based Sensors in Biological Fluids, *Anal. Chem.*, 2021, **93**, 5849–5855.
59 H. Li, P. Dauphin-Ducharme, N. Arroyo-Currás, C. H. Tran, P. A. Vieira, S. G. Li, C. Shin, J. Somerson, T. E. Kippin and K. W. Plaxco, A Biomimetic Phosphatidylcholine-Terminated Monolayer Greatly Improves the In Vivo Performance of Electrochemical Aptamer-Based Sensors, *Angew. Chem., Int. Ed.*, 2017, **56**, 7492–7495.
60 R. Bhure, T. M. Abdel-Fattah, C. Bonner, F. Hall and A. Mahapatro, Stability of phosphonic self assembled monolayers (SAMs) on cobalt chromium (Co–Cr) alloy under oxidative conditions, *Appl. Surf. Sci.*, 2011, **257**, 5605–5612.
61 N. Phares, R. J. White and K. W. Plaxco, Improving the Stability and Sensing of Electrochemical Biosensors by Employing Trithiol-Anchoring Groups in a Six-Carbon Self-Assembled Monolayer, *Anal. Chem.*, 2009, **81**, 1095–1100.